Steep Shelf Stabilization of the Coastal Bransfield Current: Linear Stability Analysis

F. J. POULIN

Department of Applied Mathematics, University of Waterloo, Waterloo, Ontario, Canada

A. STEGNER

Laboratoire de Météorologie Dynamique, École Polytechnique, Palaiseau, France

M. HERNÁNDEZ-ARENCIBIA, A. MARRERO-DÍAZ, AND P. SANGRÀ

Departamento de Física, Universidad de Las Palmas de Gran Canaria, Campus Universitario de Tafira, Las Palmas, Spain

(Manuscript received 8 July 2013, in final form 7 November 2013)

ABSTRACT

In situ measurements obtained during the 2010 COUPLING cruise were analyzed in order to fully characterize the velocity structure of the coastal Bransfield Current. An idealized two-layer shallow-water model was used to investigate the various instability processes of the realistic current along the coastal shelf. Particularly studied is how the topographic parameter To (ratio between the shelf slope and the isopycnal slope of the surface current) impacts the growth and the wavelength of the unstable perturbations. For small bottom slopes, when the evolution of the coastal current is controlled by the baroclinic instability, the increase of the topographic parameter To yields a selection of smaller unstable wavelengths. The growth rates increase with small values of To. For larger values of To (To $\gtrsim 10$, which is relevant for the coastal Bransfield Current), the baroclinic instability is strongly dampened and the horizontal shear instability becomes the dominant one. In this steep shelf regime, the unstable growth rate and the wavelength selection of the baroclinic coastal current remains almost constant and weakly affected by the amplitude of the bottom velocity or the exact value of the shelf slope. Hence, the linear stability analysis of an idealized Bransfield Current predicts a typical growth time of 7.7 days and an alongshore scale of 47 km all along the South Shetland Island shelf. The fact that these large growth times are identical to the typical transit time of water parcels along the shelf may explain why the current does not exhibit any unstable meanders.

1. Introduction

Coastal currents are important features of the local or the regional circulation that control the cross-shelf transport. If these currents are unstable, large meanders may grow and lead to the formation of coherent eddies that will capture and transport important water masses for a long time (from months to years) over large distances. On the other hand, a stable coastal jet will act as a dynamical barrier and may strongly reduce the cross-shelf transport. Hence, the stability of buoyant coastal flows has a crucial impact on the salinity, heat, and buoyancy budget or the redistribution of nutrient-rich coastal waters toward the open sea. Many density-driven coastal currents such as the Algerian Current (Millot 1999; Obaton et al. 2000), the West Greenland Current (Eden and Boning 2002; Pickart et al. 2005), and the Norwegian Coastal Current (Bjork et al. 2001) shed coherent and long-lived eddies along the coast (Puillat et al. 2002; Hatun et al. 2007). The formation of these mesoscale eddies are generally due to current instabilities (Obaton et al. 2000; Pennel et al. 2012) or bathymetric variations (Bracco and Pedlosky 2003; Bracco et al. 2008). On the other hand, a few buoyant coastal flows appear to be stable and almost stationary. The coastal Bransfield Current, which flows along the steep shelf of the South Shetland Island in Antarctica, seems to be one of them. Indeed, according to many surveys (Niiler et al. 1991; Zhou et al. 2002, 2006; Savidge and Amft 2009; Sangra et al. 2011), this current always follows the same path above the coastal shelf and large meanders were never observed.

Corresponding author address: Francis Poulin, Department of Applied Mathematics, University of Waterloo, 200 University Ave. W., Waterloo, ON N2L 3G1, Canada.
E-mail: fpoulin@uwaterloo.ca

DOI: 10.1175/JPO-D-13-0158.1

The primary goal of this study is to ascertain whether the steep bathymetry of the coastal shelf can account for the robustness and the apparent stability of the coastal Bransfield Current. To do so, we first need to quantify the relevant dynamical parameters of the current. Hence, we performed various in situ measurements during the 2010 COUPLING cruise and characterized the velocity structure of this coastal current. Then, we developed an idealized two-layer shallow-water model to account for the various instability processes of a realistic current profile along the coastal shelf and investigate thoroughly how the shelf slope impacts the growth and wavelength of the unstable perturbations.

Several studies investigate the linear stability of a purely barotropic jet flowing above a shelflike bathymetry (Li and McClimans 2000; Poulin and Flierl 2005). The presence of the bottom topography induces a potential vorticity (PV) gradient of the barotropic layer, and, depending on the particular flow and topography, this can destabilize or stabilize the current. The coastal flow is classified here as prograde (retrograde) if the topographic Rossby waves propagate in the same (opposite) direction as the current. In the Northern Hemisphere, a prograde current leaves the coast, that is, the shallower side, on its right. Li and McClimans (2000) used the rigid lid rotating shallow-water model to perform their linear stability. They determined that the neutral curves between stability and instability for prograde and retrograde flows were symmetric and then concluded that both types of topographies had a stabilizing effect. However, they observed that the prograde topography tended to have more unstable modes. The stability analysis of Poulin and Flierl (2005) used the rotating shallow-water model with a free surface and computed the growth rates numerically. This study revealed that retrograde topography is strictly stabilizing in comparison with the flat-bottom case, whereas prograde topography will first destabilize the jet and then stabilize it when the topographic slope increases beyond a critical value. Hence, when the shelf slope is strong enough both prograde and retrograde barotropic currents will be stabilized by the coastal bathymetry. Nevertheless, the barotropic assumption cannot account for the baroclinic instability induced by the vertical velocity shear of the current.

To study the stability of coastal currents to both barotropic and baroclinic perturbations, multiple layers or continuously stratified models should be used. In the framework of quasigeostrophic (QG) models, both the two-layer model (Mysak 1977) and the continuously stratified Eady model (Blumsack and Gierasch 1972; Mechoso 1980) show that a prograde current, which corresponds to a negative shelf slope (i.e., shelf slope and isopycnals tilt in the opposite sense), reduces the unstable growth of baroclinic modes. These idealized studies demonstrate that the central parameter of the problem is $\mathrm{To} = s/\alpha$, the ratio of the bottom slope s over the isopycnal slope α. However, these quasigeostrophic models are oversimplified and their predictions may not be valid for steep slope configurations. Hence, recent studies generally used two-layer shallow-water equations or the hydrostatic primitive equations to model the unstable dynamics of the coastal current over sloping bathymetry. In this context, the linear stability analyses of Lozier et al. (2002) and Lozier and Reed (2005) show that a negative shelf slope may amplify the unstable growth. We estimate the values of To used by Lozier and Reed (2005) to have magnitudes only slightly below $\mathrm{To} = -1$, and note that they may not have reached the steep slope values investigated by Pennel et al. (2012) where a significant stabilization of a coastal baroclinic front occurred. The linear stability analysis performed by Gula and Zeitlin (2013) with a two-layer shallow-water model shows that for negative shelf slopes the most unstable growth rates may increase for moderate $\mathrm{To} \simeq -1$ and then decrease for steeper values $\mathrm{To} \leq -2$. Nevertheless, the topographic slope parameter To is not the only dynamical parameter that controls the geostrophic baroclinic instability (Phillips 1954; Mysak 1977) and other ageostrophic instabilities (Sakai 1989; Gula et al. 2010) of coastal currents. The growth of these various unstable modes will also depend on the Rossby number and the vertical stratification. Hence, a careful investigation of the parameter space is needed to quantify accurately the growth rates of unstable perturbations for a realistic current flowing along a coastal shelf.

In the present paper, we restrict our linear stability analysis to the parameters of the coastal Bransfield Current. The dynamical parameters of this surface-intensified current, namely the Rossby number Ro, the vertical aspect ratio $\gamma = H_1/H_2$ (the ratio of the upper- and lower-layer depths, respectively) that characterizes the vertical structure of the flow, and the Burger number Bu, are deduced from various in situ measurements [ADCP, expendable current profiler (XCP), surface drifters, and CTD] analyzed in section 2. Section 3 explains the idealized two-layer shallow-water model we used and the choice of the hyperbolic tangent profile to mimic the coastal shelf topography along the South Shetland Islands. The results of the linear stability analysis are presented in section 4 for various shelf slopes. The impact of the shelf topography on the stabilization/destabilization of the coastal Bransfield Current is investigated by varying To from a flat-bottom configuration ($\mathrm{To} = 0$) to a steep shelf slope ($\mathrm{To} = -18$). Moreover, we perform a detailed analysis of the barotropic/baroclinic

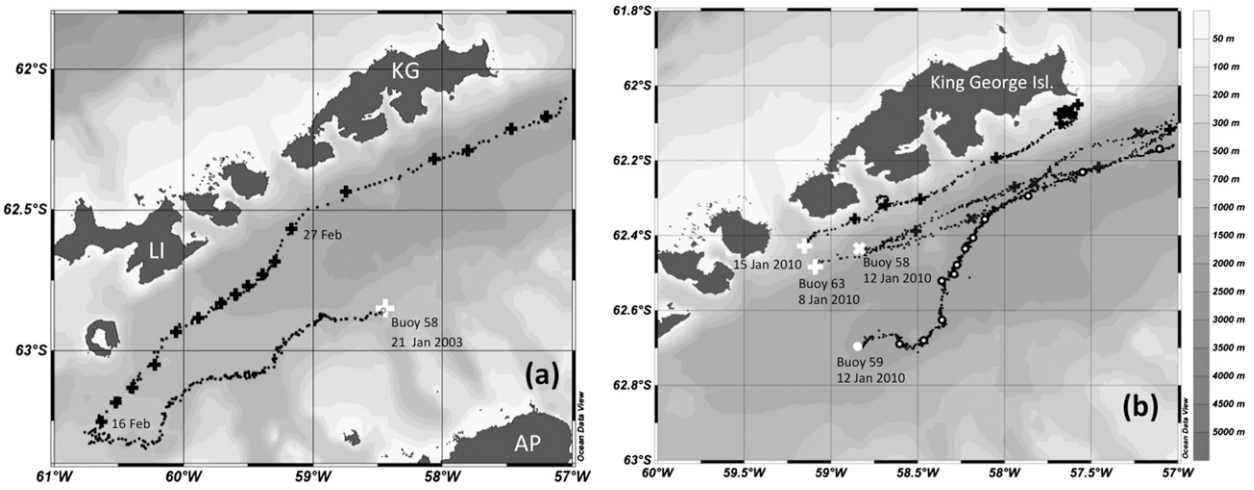

FIG. 1. Drifter trajectories launched in the Bransfield Strait during the (a) BREDDIES cruise in 2003 and the (b) COUPLING cruise in 2010. The white symbols correspond to the launching positions and black symbols (crosses, open circle) correspond to daily positions. KG, LI, and AP denote King George Island, Livingston Island, and the Antarctic Peninsula, respectively.

nature of the instability. Last, in section 5, we discuss the relevance and the limitations of this linear analysis to predict the meandering of the coastal Bransfield Current.

2. Characteristics of the Coastal Bransfield Current

The Bransfield Strait is a semienclosed basin located between the steep shelf of the South Shetland Islands (SSI) and the tip of the Antarctic Peninsula (Figs. 1, 2). The central basin is deeper than 1400 m with a main cyclonic circulation. Relatively warm and fresh water from the Bellingshausen Sea, also called transitional zonal water with Bellingshausen Sea influence (TBW), flows northeastward along the southern shelf of the SSI, whereas the cold and salty water from the Weddell Sea circulates southwestward along the irregular bathymetry of the peninsula tip in the southern half of the strait. The northeastward flow that shows the strongest velocities in the strait is known as the Bransfield Current or the Bransfield Front (Niiler et al. 1991; Zhou et al. 2002, 2006; Savidge and Amft 2009; Sangra et al. 2011).

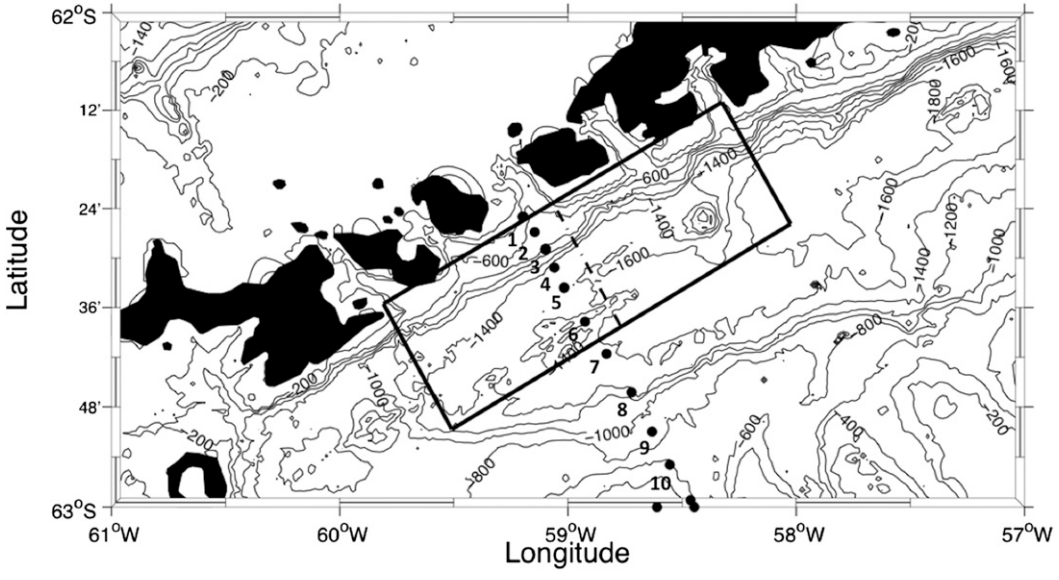

FIG. 2. From the 2-Minute Gridded Global Relief Data (ETOPO2), bathymetry along the South Shetland Islands. The black dots correspond to the location of vertical CTD profiles taken along the transect T1b from 8 to 11 Jan 2010. The mean shelf bathymetry, used below (Fig. 6c), was averaged along the coast in the black square zone.

According to previous observational studies that used the statistical mean of surface drifters (Zhou et al. 2002) or historical ADCP data (Savidge and Amft 2009), it has been determined that the Bransfield Current has a maximum surface speed around 40 cm s^{-1}. The alongslope geostrophic transport induced by this current could reach values up to 0.7–0.9 Sverdrups (Sv; 1 Sv $\equiv 10^6$ m^3 s^{-1}) (Sangra et al. 2011). An idealized laboratory model compared to field observations suggests that the Bransfield Current behaves as a density-driven gravity current (Sangra et al. 2011). In such cases, the maximum speed of the current would be located off the coast at approximately one deformation radius, which is around 10 km for this region (Chelton et al. 1998). To better quantify the horizontal and the vertical structure of the coastal Bransfield Current, we collected, during the 2010 COUPLING cruise, various velocity measurements (ADCP, XCP, and surface drifters) and high-resolution hydrographic sampling along the south SSI shelf.

a. *Surface drifters' trajectories along the south coastal shelf of the South Shetland Islands*

The surface drifters we used consisted of spherical surface floats and holey-sock drogues centered at 100 m for the BREEDIES cruise (Fig. 1a) and 50 m for the COUPLING cruise (Fig. 1b). The drogue depth was chosen so that the buoys followed the motion of water parcels below the surface mixed layer in order to reduce the impact of the wind-driven or Ekman currents on the drifters' trajectories. Each buoy was tracked by the Argos Data Collection and Location System (DCLS) every 1–2 h with an accuracy better than 500 m, which allows for the resolution of the slow mesoscale dynamics and the fast inertial motion. However, in order to quantify the mean current velocities from drifter trajectories, a 36-h low-pass filter was applied to remove the inertial or the tidal oscillations.

Among the few drifters deployed during the BREEDIES cruise in 2003 (Sangra et al. 2011), buoy 58, initially released in the middle of the Bransfield Strait on 21 January, was trapped inside the Bransfield Current in mid-February and followed the coastal SSI shelf for 16 days (Fig. 1a). During the COUPLING cruise in 2010, three drifters (buoys 63, 58, and 57) were released inside the Bransfield Current, respectively on 8, 12, and 15 January and they all followed a rectilinear trajectory along the coastal shelf for 4–6 days up to the southeastern tip of King George Island (Fig. 1b). A fourth drifter (buoy 59), released 12 January in the middle of the basin, was close to the coastal shelf 1 week later and then exhibited a linear path as with the previous buoys. In agreement with the previous drifter analysis of Zhou et al. (2002), we confirm here that once they are trapped inside the coastal Bransfield Current all the drifters tend to follow a rectilinear trajectory along the south continental margin of the South Shetland Islands (Fig. 2). Hence, the Bransfield Current does not exhibit any significant meanders above the steep coastal shelf and seems to be relatively stable in the summer months.

b. *Velocity measurements*

To more accurately quantify the vertical velocity structure of the Bransfield Current, several Sippican XCPs were launched along the transect T1b shown in Fig. 2. These expendable probes provide almost real-time profiles of current speed and direction from the ocean surface to depths of up to 1500 m with a vertical resolution of 0.4 m. Such deep and high-resolution measurements of horizontal velocities can hardly be achieved with standard boat ADCP. Unfortunately, only three profilers worked properly and provided reliable data. Two of them, XCP-02 and XCP-18, were launched 8 and 12 January, respectively, in the center of the current (position 3: 62.42°S, 59.16°W) 9 km away from the coast, while the third one, XCP-03, was launched 8 January in the outer edge of the current (position 5: 62.54°S, 59.03°W), 170 km away from the coast. The barotropic velocity of the XCP raw data was adjusted in order to match the mean surface velocity between the XCP and the boat ADCP signal in the first 100 m. From these XCP measurements, we obtain the along- and cross-shore components of the velocity down to 700–1200 m. The cross-shore velocities, averaged along the vertical, never exceed 1/5 of the velocity amplitude, therefore we plot only the alongshore velocity profiles in Fig. 3. A low-pass filter was used to separate the mean vertical velocity shear (thick line in Fig. 3) from the small vertical fluctuations (5–50 m) induced by internal gravity waves. These vertical XCP profiles confirm the baroclinic structure of the Bransfield Current. The highest speeds of 30–40 cm s^{-1} are reached at the surface, while close to the seafloor the velocity does not exceed 5 cm s^{-1}. The mean deep-layer velocity, averaged from 250 m to the bottom, appears to be small (7.4, −0.2, and 8.4 cm s^{-1} for XCPs 18, 02, 03) in comparison with the surface velocity. Hence, in what follows, we will focus the analysis on the mean surface velocity averaged in the top 100 m.

Assuming a quasi-stationary current, we combine the various measurements taken at different times during the first two weeks of January 2010 in Fig. 4. The mean surface velocities (averaged over the first 100 m) derived from the drifter trajectories, the boat ADCP (in stations and during navigation), and the XCP profiles give a first estimate of the horizontal structure of the Bransfield Current along the coast. An approximate fit is given by the equation

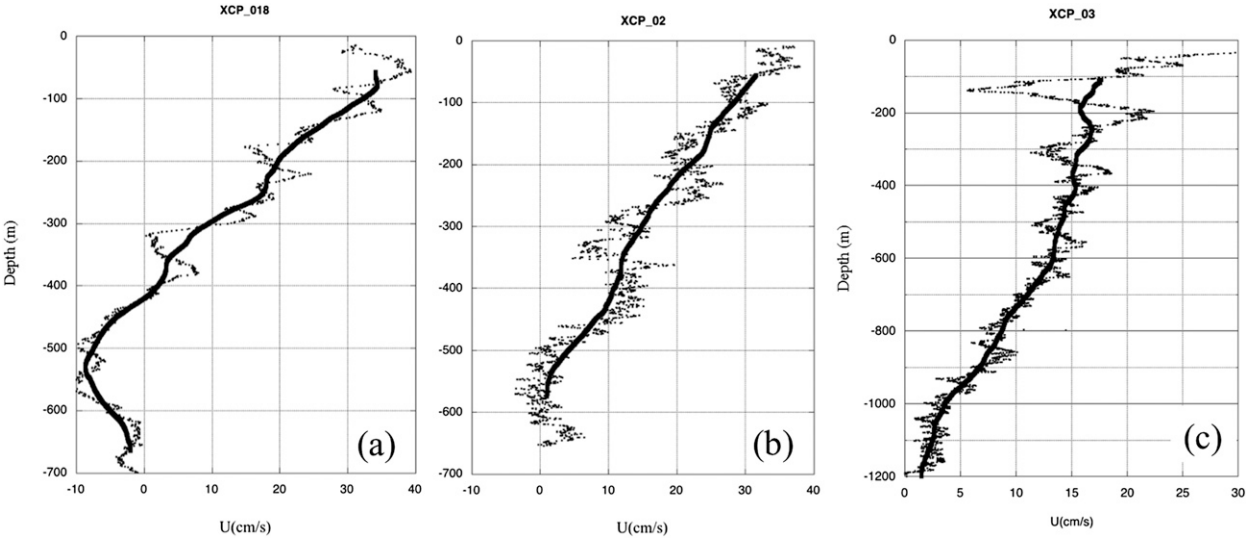

FIG. 3. Alongshore velocity profiles measured from XCP within the coastal Bransfield Current taken in position 3 at (a) 1643 LT 8 Jan and (b) 1016 LT 12 Jan and at position 5 at (c) 1435 LT 8 Jan. The thick line corresponds to smoothed profiles, low-pass filtered with 100-m cutoff.

$$V(x) = \frac{U_0}{L_0} y \exp\left[\frac{y}{L_0}\left(1 - \frac{y}{L_0}\right)\right], \qquad (1)$$

where x is the distance to the mean SSI coastline. This compilation of data shows that the maximum alongshore velocity $U_0 = 30$–$40\,\mathrm{cm\,s^{-1}}$ is located at $L_0 \simeq 10\,\mathrm{km}$ from the coast. We can then estimate the corresponding Rossby number

$$\mathrm{Ro} = \frac{U_0}{fL_0} \simeq 0.25.$$

We confirm here that the coastal Bransfield Current is a narrow, geostrophic jet propagating along the SSI shelf with a strong baroclinic shear corresponding to surface-intensified flows. The vertical and horizontal structures of this coastal jet, with a maximum speed located at approximately one deformation radius ($R_d \simeq 10\,\mathrm{km}$) from the coast, are both in agreement with the dynamical characteristics of a density-driven gravity current (Sangra et al. 2011).

c. *Vertical density structure of the coastal current*

The 13 CTD profiles of the transect T1b (Fig. 2) were taken between 8 and 11 January 2010. The horizontal sampling is about 5 km above the SSI shelf and 10 km in the center of the Bransfield Strait, whereas the vertical resolution is close to 1 m. From these high-resolution measurements, we extracted a vertical density section across the strait (Fig. 5). The low density of the surface waters corresponds to warm and freshwater from the Bellingshausen Sea (i.e., TBW). Because of the gradient wind balance, the Bransfield Current induces a significant isopycnal tilting along the SSI coast (distance 0–20 km in Fig. 5). The thermocline depth of TBW is about 100–150 m in the central basin and goes down to 300–350 m at the SSI coast, with a maximum slope around $\alpha \simeq 1\%$. On the other

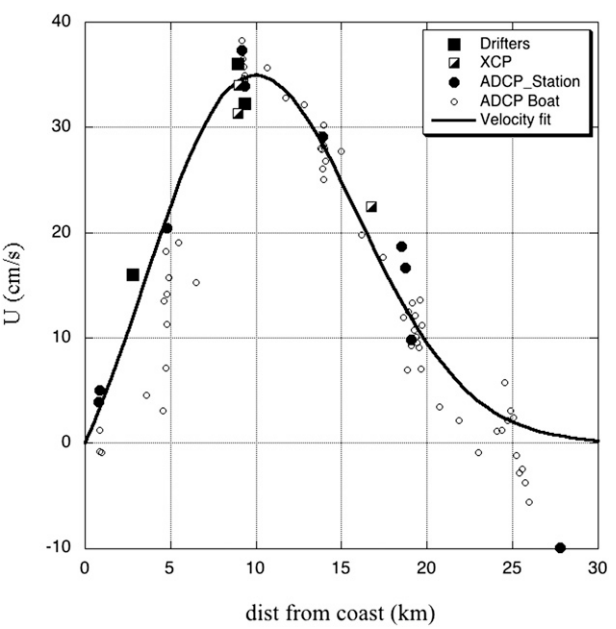

FIG. 4. Surface velocity measurements across the transect T1b from 8 to 11 Jan 2010. ADCP velocity measurements, averaged in the first 100 m, are plotted with open circles (moving boat) and filled circles (boat on station). Few XCPs were taken, and the surface velocity averaged in the first 100 m is plotted with semifilled squares. The mean surface velocity deduced from the three Argos drifter (buoys 57, 58, and 63) trajectories is plotted with filled squares. The black solid line corresponds to the empirical fit given by Eq. (1).

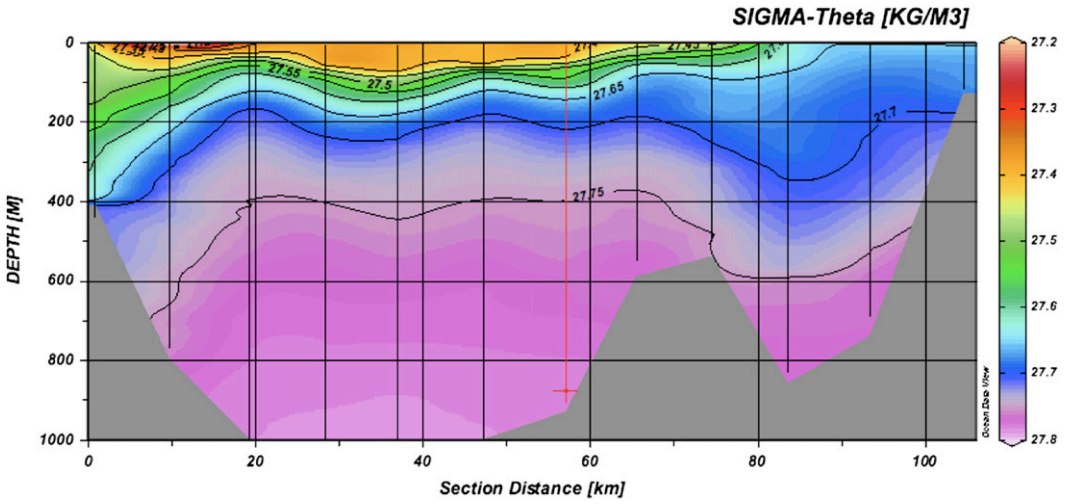

FIG. 5. Vertical cross section of the potential density anomaly along the transect T1b. This vertical section was computed from 13 CTD profiles taken from 8 to 11 Jan 2010. The gray area corresponds to regions without measurements; the bottom shelf is below this limit.

side of the strait, close to the Antarctic Peninsula, the thermocline outcropping (distance 70–80 km in Fig. 5) is a signature of the peninsula front. It separates the well-stratified and light TBW from the homogeneous and relatively dense transitional zonal water with Weddell Sea influence (according to Sangra et al. 2011). Previous surveys of this region revealed similar density sections (Garcia et al. 1994; Basterretxea and Aristegui 1999; Sangra et al. 2011).

3. A two-layer model

Observations of the Bransfield Current clearly indicate that it is very regular, is surface intensified, and has relatively little vertical variation in the upper 100 m. This, in part, motivates us to idealize this current using rotating shallow-water (RSW) dynamics. In particular, we take a two-layer model, where the upper layer contains the strong surface current and the lower layer is assumed to be either motionless (but still dynamic) or relatively weak compared to the layer above. The lower layer completely covers the topography, by which we mean that the surface current does not interact directly with the topography but only indirectly through the dynamics of the lower layer. In this section, we first present the model equations, discuss important nondimensional parameters, and then state the numerical method that we use to solve for the characteristics of the linear stability problem numerically. The results of the stability analysis are presented in the next section.

a. Semirealistic shelf bathymetry

We can use either direct in situ measurements or a bathymetric database to determine the bottom topography in the lower layer of our model. The topography along the transect T1b, measured at high resolution by the boat echo sounder, is plotted in Fig. 6b, while the idealized velocity profile of the surface current is shown in Fig. 6a. The highest current speed is located just above the shelf break very close to the maximal bottom slope. However, in order to avoid numerical noise and spurious results in the linear stability analysis, we need to smooth out small-scale topographic fluctuations. Hence, we perform a spatial averaging ETOPO2 along the South Shetland Islands. We do so within a rectangular band, the black box shown in Fig. 2, that is 120 km long and 35 km wide. The alongshore averaging of the shelf topography (Fig. 6c) fits remarkably well with the hyperbolic tangent function

$$h_B(y) = H_T + \Delta h \tanh\left[\frac{s}{\Delta h}(L_0 - y)\right], \qquad (2)$$

where $h_B(y)$ is the total water depth, y is the cross-shore coordinate defined in Eq. (1), $H_T = 900$ m is the water depth below the maximal current speed at $y = L_0 = 10$ km, $\Delta h = 600$ m is the depth variation between the central basin and the coastal plateau, and $s = -\partial_y h_B$ is the maximum shelf slope. The shelf and the isopycnals tilt in the opposite sense, and we therefore use the convention $s < 0, \alpha > 0$ for gravity-driven coastal flows. The bottom slope $s \simeq -15\%$ is high in comparison with the isopycnal slope $\alpha \simeq 1\%$ of the surface current; the topographic parameter $\mathrm{To} \simeq -15$ is large and therefore the coastal Bransfield Current corresponds to a steep shelf slope configuration.

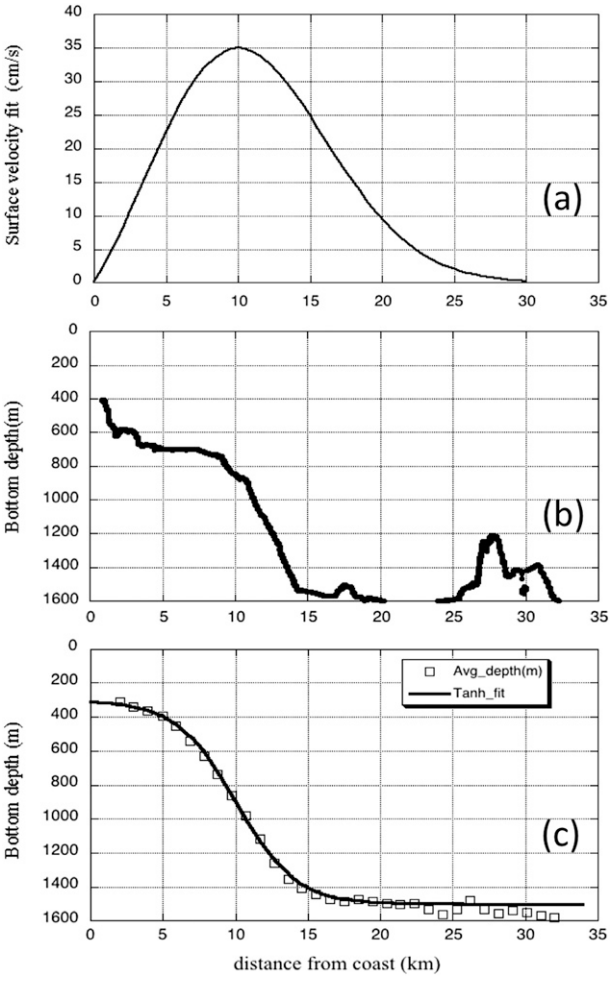

FIG. 6. (a) Idealized surface velocity profile over the bottom shelf bathymetry of the (b) transect T1b and the (c) mean shelf bathymetry averaged along the coast from ETOPO2 (see the rectangle in Fig. 2).

b. Two-layer shallow-water equations

Following convention, if we define u_1, v_1, and h_1 and u_2, v_2, and h_2 to be the velocities and layer depths for the upper and lower layers, respectively, then our governing equations can be written as

$$\frac{\partial \mathbf{u}_j}{\partial t} + (\mathbf{u}_j \cdot \nabla)\mathbf{u}_j + f\mathbf{k} \times \mathbf{u}_k = -\nabla[gh_1 + (g + \delta_{2k}g')(h_2 - h_B)] \quad \text{and} \qquad (3)$$

$$\frac{\partial h_k}{\partial t} + \nabla \cdot (h_k \mathbf{u}_k) = 0, \qquad (4)$$

in terms of the Kronecker delta function δ_{jk} where g is the full gravity and g' is the reduced gravity defined as

$$g' = \frac{\rho_2 - \rho_1}{\rho_1} g.$$

For our idealized model of the Bransfield Current, the density difference between the upper and lower layers is less than 0.1%.

The layered RSW model has been used extensively in the oceanographic literature to idealize particular processes, and the interested reader is directed to Zeitlin (2007) for a review of the literature on the subject. The spectral collocation method that we use to solve for the stability characteristics are the two-layer extensions of those previously used in Poulin and Flierl (2003, 2005).

A very useful limit of the RSW model is the QG model. This model describes the motion of a fluid whose interfaces do not change significantly in comparison to the depth of each layer. Furthermore, the superinertial gravity waves are completely filtered out. The constraint imposed by QG in regards to the interfacial deformations makes it less applicable to the Bransfield Current because the deformations in the lower layer are on the same order as the depth of the layer itself. However, we still consider QG dynamics because it can still be very descriptive in the case of weaker topography, and it is a very popular model that is often considered in oceanographic investigations.

The two-layer, inviscid, QG model with a rigid lid and variable topography, denoted again with h_B, can be described in dimensional form in terms of the evolution of the PV of each layer:

$$\frac{D}{Dt}\left[\nabla^2\psi_1 - \frac{f^2}{g'H_1}(\psi_1 - \psi_2)\right] = 0 \quad \text{and} \qquad (5)$$

$$\frac{D}{Dt}\left[\nabla^2\psi_2 - \frac{f^2}{g'H_2}(\psi_2 - \psi_1) - \frac{f_0}{H_2}h_B\right] = 0. \qquad (6)$$

Note that ψ_1 and ψ_2 are the streamfunctions, and H_1 and H_2 are the mean depths for the upper and lower layers, respectively. The PV is a sum of the relative vorticity, baroclinic stretching term due to the interfacial deformations (that is equal in magnitude but of opposite sign in the two layers), and a stretching term in the lower layer due to the topography. Note that because the length scales are relatively small compared to planetary scales, we neglect the ambient vorticity due to the meridional variation in the Coriolis force.

c. Dynamical and topographic parameters

One of the first attempts to describe the baroclinic instability was made by Phillips (1954) using a simplified two-layer QG model with uniform velocities (U_1, U_2) in both the upper and lower layers. Without any horizontal

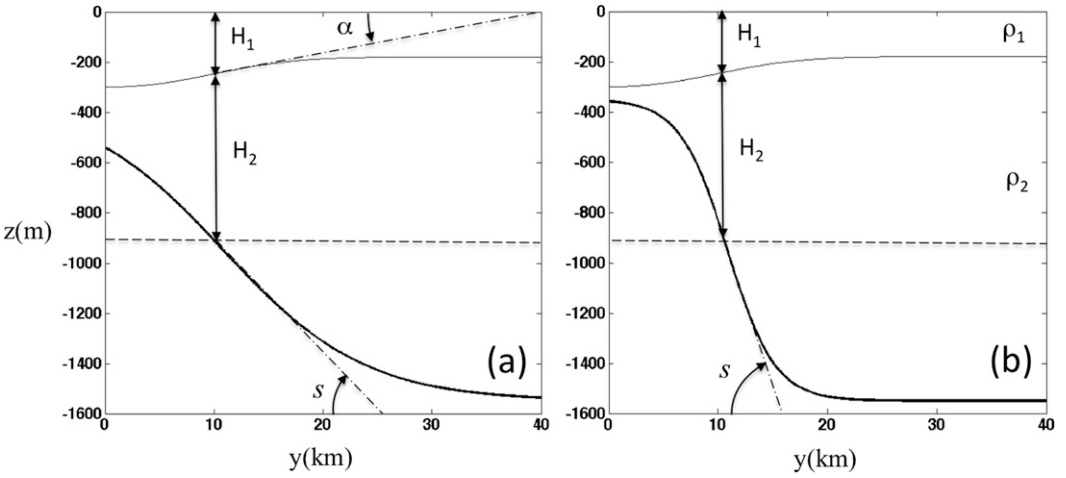

FIG. 7. Two-layer model of a surface coastal current above an idealized hyperbolic tangent bathymetry with a topographic parameter (a) To $= s/\alpha = -17$ and (b) To $= -2$. The dashed line corresponds to the flat-bottom configuration where the bottom depth is $H_1(y = L_0) + H_2(y = L_0) = H_T = 900$. The maximal isopycnal slope of the upper-layer $\alpha = 0.88\%$ and the vertical aspect ratio of the two-layer $\gamma = H_1/H_2$ are kept constant while the bottom slope varies: $s = -0.05$ in (a) and $s = -0.15$ in (b).

velocity shear this model captures only the baroclinic instability, in other words, the resonant interaction between an upper and a lower Rossby wave (Pedlosky 1987; Vallis 2006). In the framework of this simplified two-layer model, widely used to describe the baroclinic instability of oceanic currents, the growth rates are mainly controlled by the vertical aspect ratio parameter:

$$\gamma = H_1/H_2 .$$

The geometry of our model is presented in Fig. 7.

Figure 8a shows, for the QG Phillips model with $U_1 = U_0$ and $U_2 = 0$ (a motionless bottom layer), the dependency of the dimensionless growth rate curves $\sigma R_d/U_0 = F(kR_d)$ on γ in the flat-bottom configuration. The highest growth rates are found when $\gamma = 1$. For this case, a direct analogy between the Phillips model and the Eady model (linear stratification and velocity shear along the vertical) could be made. For a surface-intensified current, the upper layer is thinner than the lower one, the aspect ratio parameter γ tends to small values, and both the growth rate and the most unstable wavenumber are reduced. Note that for the Phillips model, the isopycnal slope α, that is, the intensity of the surface current, has no impact on the instability because QG is an asymptotic model in the limit of vanishing Rossby number. Hence, if we introduce a bottom slope s to this idealized model, a second parameter will then control the instability. The stability analyses of Blumsack and Gierasch (1972), Mysak (1977), and Mechoso (1980), which added a bottom shelf slope to standard QG models, show that the new relevant parameter of the problem is not the bottom slope but the topographic parameter:

$$\mathrm{To} = s/\alpha .$$

For the coastal Bransfield Current the shelf slope and the isopycnals tilt in the opposite sense, and therefore To is negative. Figure 8b shows the evolution of the growth rate curve for various topographic parameters To with $\gamma = 0.4$, which is the estimated value for the Bransfield Current. Large (negative) values of the topographic parameter induce a strong reduction of the baroclinic growth rates. Moreover, a small wavenumber cutoff occurs and the most unstable wavenumber increases significantly leading to the growth of perturbations of smaller wavelength. According to this oversimplified Phillips model with bottom slope, the typical growth rate and most unstable wavenumber for the unstable Rossby–Rossby mode of the Bransfield Current (To $\simeq -15$) should be $\sigma_{\max} R_d/U_0 \simeq 0.07$ and $k_{\max} R_d \simeq 2.6$. However, this idealized two-layer QG model is not strictly valid for significant variations of the bottom shelf (i.e., steep slopes) and cannot account for the ageostrophic Rossby–Kelvin or Rossby–gravity wave instabilities.

The RSW system is more general and can, at least in part, accurately model the above mentioned instabilities. Two other dimensional parameters control the system, namely the Rossby number and the Burger number:

$$\mathrm{Ro} = \frac{U_0}{fL_0} \quad \text{and} \quad \mathrm{Bu} = \frac{g' H_1}{f^2 L_0^2} = \left(\frac{R_d}{L_0}\right)^2 .$$

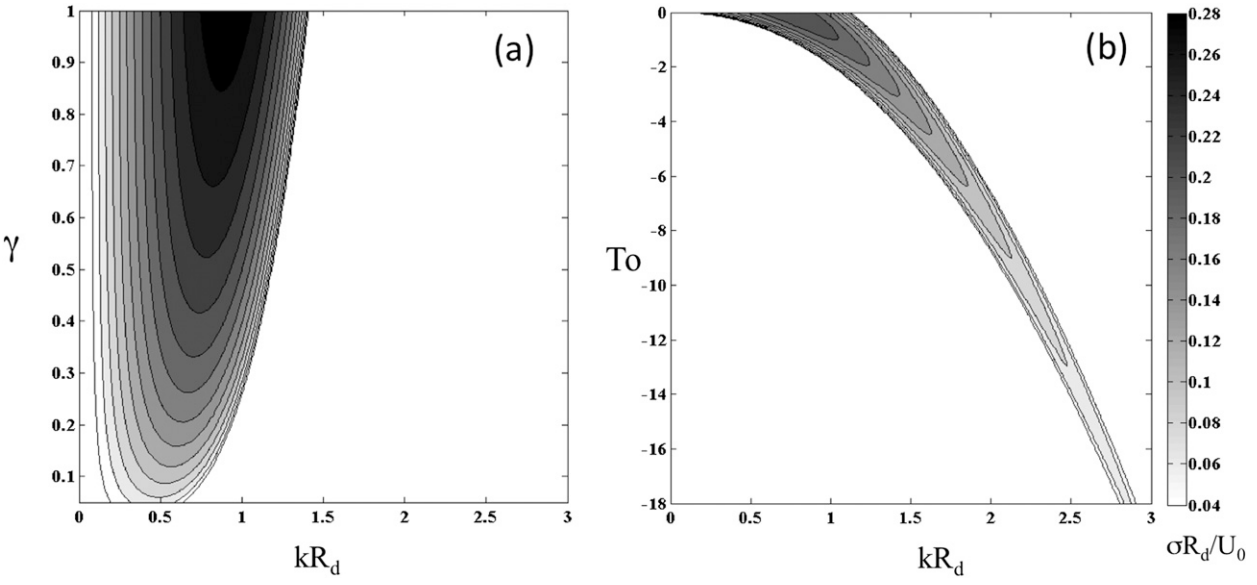

FIG. 8. Stability diagram of the QG Phillips model with a linear shelf slope in the bottom layer. Evolution of the dimensionless growth rate $\sigma R_d/U_0$ as a function of the dimensionless wavenumber kR_d for various aspect ratio $\gamma = H_1/H_2$ in the (a) flat-bottom case and for (b) various topographic parameters To when $\gamma = 0.4$.

Because of the geostrophic balance of the basic state, the Rossby number is directly proportional to the isopycnal slope α by the relation $\mathrm{Ro} = \alpha \mathrm{Bu} L_0/H_1$. According to the various surveys of the Bransfield Current and the recent measurements obtained during the COUPLING cruise (see section 2), throughout this work we fix these two dynamical parameters to the values Ro = 0.25 and Bu = 0.74, which therefore yields that $\alpha = 0.88\%$.

d. Numerical methods

As previously stated, our idealization of the Bransfield Current is assumed to be described by the two-layer RSW model. We can study the stability characteristics of a general basic state whose layer depths only vary in the across-shelf direction y and has velocity profiles that are in geostrophic balance:

$$fU_1 = -g\frac{d}{dy}(H_1 + H_2 - h_B) \quad \text{and} \tag{7}$$

$$fU_2 = -\frac{d}{dy}[gH_1 + (g + g')(H_2 - h_B)], \tag{8}$$

where U_1, H_1 and U_2, H_2 are the alongshore velocities and thickness of the upper and lower layers, respectively. In the case of a flat free surface, that is, $H_1(y) + H_2(y) = h_B(y)$, the upper layer will be motionless. In most of our calculations we investigated a lower layer at rest ($U_2 = 0$) that leads to $H_2(y) = h_B(y) - (\rho_1/\rho_2)H_1(y)$.

For most of our analysis, we consider flows with a motionless lower layer. This is in contrast to the observations that indicate that there is a weak mean flow at depth; however, the variance in the observations indicate that we do not know the details well enough to prescribe it correctly. That is why we have chosen to neglect this unknown for part of our analysis but revisit this issue at the end of section 4.

We perturb the basic state with infinitesimal disturbances that allow us to linearize the governing evolution equations

$$[u_j, v_j, h_j] = [U_j + u_j', V_j + v_j' H_j + h_j'], \tag{9}$$

for the indices $j = 1, 2$. Next, we assume a normal-mode decomposition in the alongshore direction and time:

$$[u_j', v_j', h_j'](x, y, t) = \mathrm{Re}\{e^{ik(x-ct)}[\hat{u}_j, ik\hat{v}_j, \hat{h}_j](y)\}. \tag{10}$$

Note that the choice of including a factor of ik in front of the cross-channel velocity is to ensure that the resulting eigenvalue problem is strictly real in the inviscid limit and therefore can speed up the time it takes to compute the spectrum of the system.

When we substitute this decomposition into the governing equations and simplify, we obtain the following system of six equations that form the eigenvalue problem and therefore the stability characteristics of the basic state:

$$c\hat{u}_1 = U_1\hat{u}_1 - \left(f - \frac{dU_1}{dy}\right)\hat{v}_1 + g(\hat{h}_1 + \hat{h}_2) + \frac{i\nu}{k}(k^2 - \partial_{yy})\hat{u}_1, \tag{11}$$

$$c\hat{v}_1 = -\frac{f}{k^2}\hat{u}_1 + U_1\hat{v}_1 - \frac{g}{k^2}\frac{d}{dy}(\hat{h}_1 + \hat{h}_2) + \frac{i\nu}{k}(k^2 - \partial_{yy})\hat{v}_1, \tag{12}$$

$$c\hat{h}_1 = H_1\hat{u}_1 + \frac{d}{dy}(H_1\hat{v}_1) + U_1\hat{h}_1 + \frac{i\kappa}{k}(k^2 - \partial_{yy})\hat{v}_1, \tag{13}$$

$$c\hat{u}_2 = g\frac{\rho_1}{\rho_2}\hat{h}_1 + U_2\hat{u}_2 - \left(f - \frac{dU_2}{dy}\right)\hat{v}_2 + g\hat{h}_2 + \frac{i\nu}{k}(k^2 - \partial_{yy})\hat{u}_2, \tag{14}$$

$$c\hat{v}_2 = -\frac{g}{k^2}\frac{\rho_1}{\rho 2}\frac{d\hat{h}_1}{dy} - \frac{f}{k^2}\hat{u}_2 + U_2\hat{v}_2 - \frac{g}{k^2}\frac{d\hat{h}_2}{dy} + \frac{i\nu}{k}(k^2 - \partial_{yy})\hat{v}_2 \quad \text{and} \tag{15}$$

$$c\hat{h}_2 = H_2\hat{u}_2 + \frac{d}{dy}(H_2\hat{v}_2) + U_2\hat{h}_2 + \frac{i\kappa}{k}(k^2 - \partial_{yy})\hat{h}_2. \tag{16}$$

These equations are discretized numerically using spectral collocation on a Chebyschev grid to achieve spectral accuracy as done in the one-layer case in Poulin and Flierl (2003, 2005) based on the methods beautifully presented in Trefethen (2000).

In the above system we have included viscous and diffusive processes in the model whose strength is set by ν and κ, respectively, both equal to 0.1. To our knowledge using dissipative forces in this spectral collocation method for the RSW is novel. This is computationally more expensive because the resulting system is complex; however, the advantage is that the dissipative forces reduce the weak numerical instabilities that can arise in these types of problems. Because of the higher order of the dissipative system, in addition to the no-normal-flow boundary conditions at the two ends of the domain, we also impose no-flux boundary conditions on the along-shelf velocity and the layer depths.

If a similar decomposition is applied to the two-layer QG system, then what results is a generalized eigenvalue problem that only has two equations and therefore is less computationally expensive to analyze:

$$c\{[\partial_{yy} - (k^2 + F_1^2)]\hat{\psi}_1 + F_1^2\hat{\psi}_2\} = \{U_1[\partial_{yy} - (k^2 + F_1^2)]\hat{\psi}_1 + H_1Q_y^1\hat{\psi}_1 + F_1^2U_1\hat{\psi}_2\} \quad \text{and} \tag{17}$$

$$c\{F_1\hat{\psi}_1 + [\partial_{yy} - (k^2 + F_1)]\hat{\psi}_2\} = \{F_2U_2\hat{\psi}_1 + U_2[\partial_{yy} - (k^2 + F_2)]\hat{\psi}_2 + H_2Q_y^2\hat{\psi}_2\}, \tag{18}$$

where the PV gradients are defined as

$$H_1Q_y^1 = [-\partial_{yy}U_1 + F_1^2(U_1 - U_2)] \quad \text{and} \tag{19}$$

$$H_2Q_y^2 = [-\partial_{yy}U_2 + F_2^2(U_1 - U_2) - (f_0/H_2)\partial_y h_B]. \tag{20}$$

Note that we defined the inverse of the Rossby radii as $F_1^2 = f_0^2/(g'H_1)$ and $F_2^2 = f_0^2/(g'H_2)$.

In all of the results computed in the context of the RSW we used a grid of $N = 400$ Chebyschev points, whereas for the QG we were able to use $N = 1000$ because of the smaller number of equations in the system. The fact that in the flat-bottom case the results are almost identical suggests that numerical convergence has been achieved. To confirm the numerical convergence of our results we also adapted our model to solve a sparse second-order finite-difference system using indirect Krylov space methods that are much less expensive computationally. There we managed to use $N = 12\,000$ points in our linear stability calculation. The growth rates for the flat-bottom case were essentially identical and only one unstable mode was determined, confirming the validity of our results.

4. Results of the linear stability analysis

a. The impact of topography on the growth rate curves

Figure 9 consists of eight different subplots that help to illustrate how the growth rates of the Bransfield Current depend on variable topography. In the left column we have the results from the stability calculations using the QG model and in the right column we have the analog for the RSW model. The RSW model is more general than QG in that it allows for the following: 1) both isopycnal and bathymetric variations can be finite, and 2) it contains inertia gravity waves and therefore allows for ageostrophic instabilities (Sakai 1989; Gula et al. 2010). We present the stability characteristics of the QG and RSW models together in order to make a direct and visual distinction between the geostrophic and ageostrophic unstable modes. The later could only be present in the RSW model.

The four rows (starting from the top) are the stability results for the cases with the shelf slope $s = 0.00$, 0.01, 0.05, and 0.15, which correspond roughly to To = 0, −1.1, −5.7, and −17. The first row represents a flat bottom and,

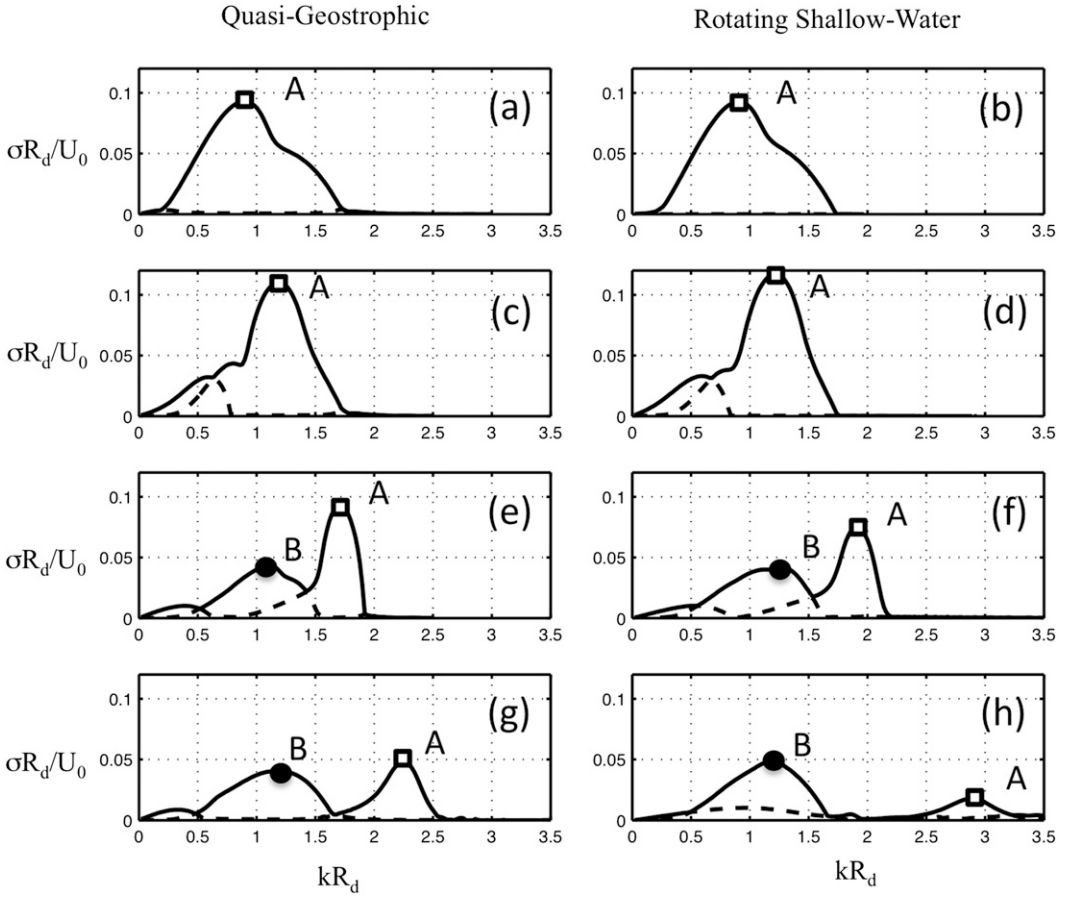

FIG. 9. The dimensionless growth rate curves as a function of dimensionless wavenumber are plotted for the (left) QG and (right) RSW models. The topographic parameters are (a),(b) To = 0, (c),(d) To = −1.1, (e),(f) To = −5.7, and (g),(h) To = −17.

even though the interfacial deformations are comparable to the layer depth itself, we see that the growth rates predicted for the most unstable modes for the QG and RSW results are virtually identical; hence, there is no evidence of any ageostrophically unstable modes for this choice of parameters in the RSW system (Fig. 9b). Indeed, according to Sakai (1989) and Gula et al. (2010) the Rossby–Kelvin and Rossby–gravity wave resonances occur for larger Rossby numbers in the flat-bottom configuration. There is only one mode[1] that is present and it is labeled *A*. The maximum growth rate, marked with an open square, is slightly less than $\sigma_{\max}U_0/R_d = 0.1$, and the most unstable mode is approximately $k_{\max}R_d = 0.9$.

The second row corresponds to very weak topography (To = −1.1), and the surface current is prograde. As found in Poulin and Flierl (2005) for a barotropic jet, the slight topography is destabilizing, in that the growth rate of the most unstable mode increases up to $\sigma_{\max}U_0/R_d = 0.12$ and the wavelength moves to slightly smaller scales of $k_{\max}R_d = 1.2$. Similar behavior was found in Lozier and Reed (2005) where the growth rate of a baroclinic shelf-break front increases above a hyperbolic tangent bathymetry. Again, the QG and RSW model seem to give results that are in good agreement even if the growth rate of the most unstable mode is slightly underestimated in the QG model. Interestingly, we find that in the presence of topography there are regions where at the large scale there are two unstable modes; these are indicated by the dashed lines.

The third row has stronger topography (To = −5.7), but one that is weaker compared to what is observed beneath the Bransfield Current. In this regime there are three different modes that are apparent. The dominant

[1] Note that the dashed line that is barely apparent in the top row is believed to be a numerical error because when we increased the resolution we found that the growth rate of this curve decreased. Since we were not able to confirm any convergence, we believe this negligible mode is spurious and this is consistent with the results of our very high-resolution calculations using Krylov space techniques.

mode, which we still call *A,* is stabilized by the topography, and the wavelength of this most unstable mode is smaller compared to the flat-bottom case. We readily observe that QG overestimates the growth rate and the horizontal length scale of this mode. There is a second mode that remains near $kR_d = 1.0$ and is labeled *B*. In both QG and RSW models the maximum growth rate of this mode *B* is $\sigma_{\max}U_0/R_d = 0.04$, denoted with a filled circle, and is weaker than the most unstable mode *A*. At larger scales $kR_d \approx 0.5$, there is a third unstable mode that is much weaker than the other two.

The fourth and final row has steep topography (To = −17) that is of the same order as what is measured below the Bransfield Current. In both QG and RSW models, this steep shelf slope reduces significantly the growth rates of mode *A*. In the RSW model, the second mode *B* is now the dominant mode, whereas in the QG model this mode has very similar growth rates to that of mode *A*. The transition from mode *A* to mode *B* indicates that there is probably a change in the nature of the instability due to the topography in both QG and RSW models. Hence, these two unstable modes are geostrophically balanced. However, in order to clarify the underlying mechanisms of instability related to modes *A* and *B,* we need to perform a more thorough analysis, which we do in the following subsection.

b. *Why mode A corresponds to baroclinic instability*

Figure 10a depicts the variation of the most unstable growth rates as a function of the topographic parameter To of modes *A* (open square) and *B* (filled circle) in the RSW model, while the solid line gives the prediction of the classical two-layer QG Phillips model [see the appendix of Pennel et al. (2012) for the details]. Fig. 10b then shows the corresponding wavelength selection as a function of To for the most unstable modes listed above and also includes a dashed line that shows the unique wavenumber solution that allows matching of the phase speed of the QG Rossby waves in the upper and lower layers (see our appendix for further details).

According to Fig. 10b, the variation of the most unstable wavelength of mode *A* is in surprisingly good agreement with that predicted from the idealized Phillips model that only allows for QG Rossby–Rossby resonant wave interaction between the upper and lower layers. This behavior is the first evidence that mode *A* corresponds to the standard baroclinic instability. The second piece of evidence is in Fig. 10a where the most unstable growth rate of mode *A* is, as for the QG Phillips model (solid line), significantly reduced for large topographic parameters. In contrast, the mode *B* is almost not affected by the steepness of the shelf slope. Note that the baroclinic instability (mode *A*) ceases to be the dominant mechanism of instability below To = −9. This transition should induce abrupt change in the wavelength selection of the unstable perturbations from small ($k_{\max}R_d \approx 2.3$) to large ($k_{\max}R_d \approx 1.2$) scales.

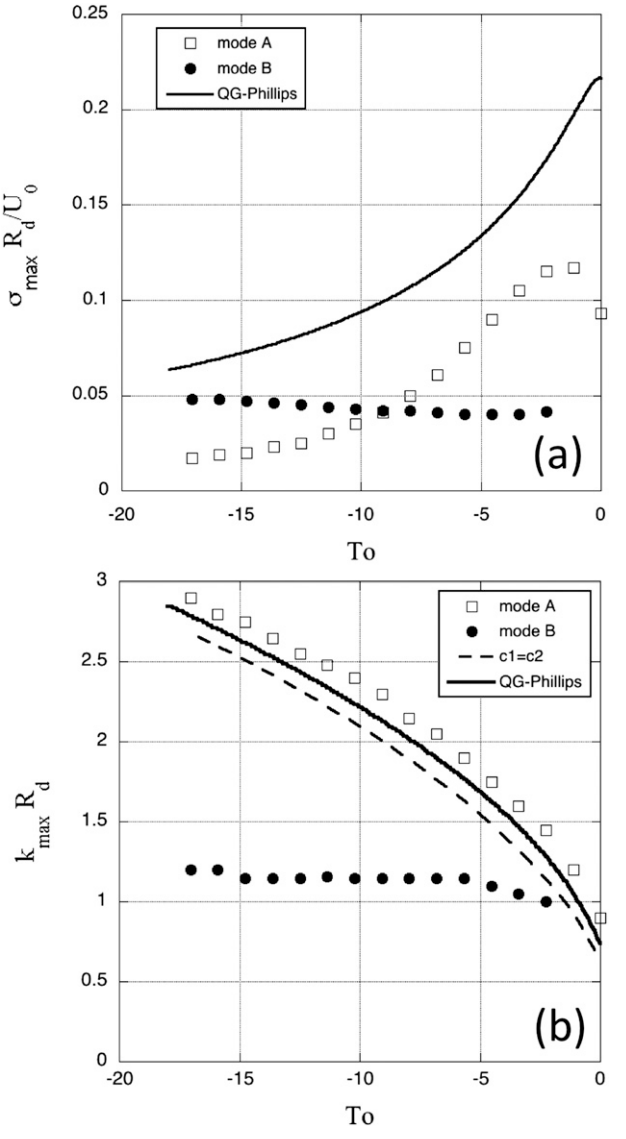

FIG. 10. Impact of the topographic parameter To on (a) the most unstable growth rates and (b) the wavelength selection for mode *A* (open squares), mode *B* (filled circles), and the QG Phillips model (solid line).

c. *Why mode B corresponds to horizontal shear instability*

Figure 11 presents the growth rates as a function of wavenumber in the presence of steep topography, as located in the Bransfield Strait (To = −17), in three different models: one-layer QG, two-layer QG, and two-layer RSW (top to bottom). Emphasis is placed on mode

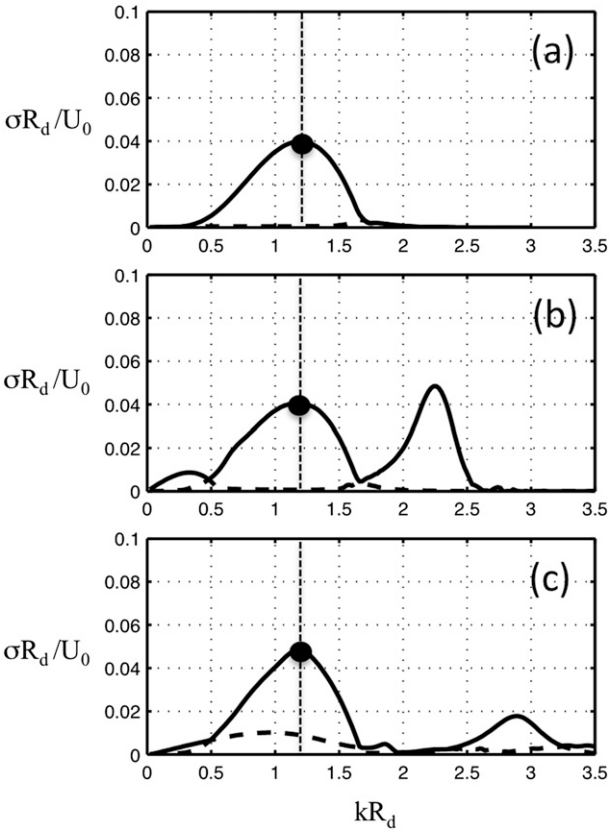

FIG. 11. The dimensionless growth-rate curves as a function of dimensionless wavenumber are plotted for the (a) one-layer QG, (b) two-layer QG, and (c) two-layer RSW models. There is no topography in (a), and the topographic parameter is To = −17 in (b) and (c).

B where a filled circle denotes the local maximal growth rate. Even though the other unstable modes vary significantly in the different models, we readily observe that the curve associated with mode *B* is very similar in the three paradigms. The maximal growth rate ($\sigma L_0/U_0 \simeq 0.045$) and the most unstable wavenumbers ($kR_d \simeq 1.2$) are almost identical in the three models. Since this mode is well described in the context of a one-layer QG model, the only possible mechanism for instability is due to the horizontal shear in the surface current. Such an instability is induced by the unstable coupling of two geostrophic shear waves that propagate on the opposite PV gradients on each side of the current. The barotropic shear instability of the longshore current was investigated by Bowen and Holman (1989) in the rigid lid approximation when the typical width of the current is much smaller than the deformation radius: $L_0 \ll R_d$. For coastal currents, when $L_0 \sim R_d$, the deviation of the internal surface cannot be neglected, and in the framework of reduced gravity 1½-layer model, Poulin and Flierl (2003) found in the QG regime that when Bu = 1 and Ro = 0.1, there are similar growth rates $\sigma_{\max}L_0/U_0 \simeq 0.05$ for the Bickley jet. Weaker growth rates and even a complete stabilization are found for the large-scale jet when L_0 becomes significantly larger than R_d, according to Perret et al. (2011). In the present case, $L_0 \sim R_d$ and the velocity profile we use for the Bransfield Current [see Eq. (1)] satisfy, as does the Bickley jet, the extended Rayleigh criterion that requires opposite PV gradients for instability of barotropic parallel flows (Pedlosky 1987; Vallis 2006). Note that if the coastal flow has a constant PV in the surface layer (Paldor 1983; Gula et al. 2010; Gula and Zeitlin 2013) the mode *B*, associated with the unstable resonance of horizontal shear modes, will not be present.

d. The spatial structure of the main unstable modes

The spatial structure of the most unstable mode *B* is shown in Fig. 12 for $kR_d = 1.2$ in both the one-layer QG model with flat bottom (Fig. 12a) and the upper (Fig. 12b) and lower (Fig. 12c) layers of the RSW model with the hyperbolic tangent shelf topography denoted in Eq. (2) with To = −17. The spatial structure of this unstable mode in the one-layer QG model (Fig. 12a) is almost identical (except for a translation in the periodic direction) to the upper-layer perturbation in the RSW model (Fig. 12b). The similarity of these spatial structures confirms that the most unstable mode *B* is driven by the instability due to the horizontal shear in the upper layer. However, even though the source of the instability is barotropic in nature (i.e., it is accurately predicted with a one-layer QG model), there is a baroclinic signature of unstable mode *B*. Considering the velocity fields only, the associated perturbation in the lower layer (Fig. 12c) is about a third weaker than that of the upper layer. We note that the cross-shore transport (v_1 velocity) is maximal where the alongshore current is strongest, $y/L_0 = 1$. In the lower layer the maximal cross-shore velocity (v_2 velocity) is closer to the coast. We have noticed that when we increase the steepness of the shelf, the perturbation associated with mode *B* changes significantly in the lower layer (the wavenumber in the cross-shore direction increases), while this is not the case in the upper layer. We found no remarkable impact of the bottom topography on the upper-layer perturbation.

The spatial structure of the most unstable mode *A* is shown in Fig. 13 for $kR_d = 2.9$ in the upper (Fig. 13a) and lower (Fig. 13b) layers of the RSW model with To = −17, which corresponds to the empty square in Fig. 9h. The two lines of rapid variation in u_1 suggest the presence of critical layers, and this has been confirmed by comparing our spectral solution with 400 grid points to the finite-difference solution with 8000 grid points. They

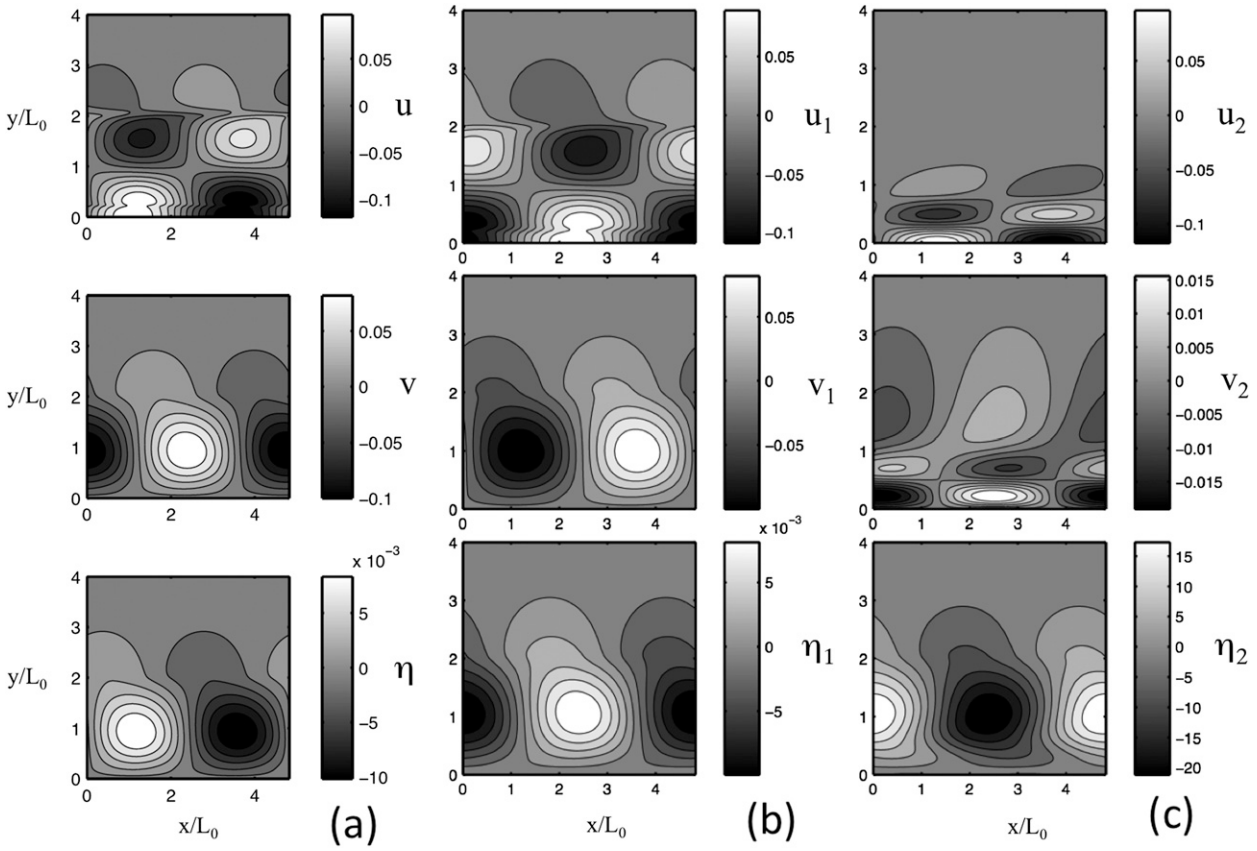

FIG. 12. Spatial structure of the most unstable mode B corresponding to $kR_d = 1.2$, the filled circles in Fig. 11: (a) one-layer QG model without any topography and (b) upper and (c) lower layers of the RSW model with To $= -17$ for the (top) alongshore velocity field, (middle) cross-shore velocity field, and (bottom) interfacial displacements. Note that the center of the mean surface current is located at $y/L_0 = 1$.

both agree, to five significant digits, that the phase speed of this mode is $-0.217\,06$, and the structure of the modes is virtually identical. Unlike mode *B,* the baroclinic nature of the perturbation is amplified by the fact that the lower-layer velocities are at least one order of magnitude larger than those in the upper layer. This is presumably because, for steep shelf slopes, the variations in the lower layer induced by the bottom topography are of the same order as the layer depth. For such a configuration, even though the mean flow is surface intensified, the unstable mode *A* is bottom intensified. Upon changing To we have found that the spatial structure of the unstable mode *A* is affected in both layers. This is in agreement with the fact that this mode is driven by the resonant coupling of Rossby waves in the upper and lower layers.

e. The impact of a weak flow in the lower layer

So far we have restricted our attention to surface coastal currents flows with no mean flows in the lower layer. The reasons to go beyond this restriction are twofold. First, according to the observations in the coastal Bransfield Current (Fig. 3), there is a weak but nonnegligible mean flow at depth. Second, our result that the growth rate and wavelength selection associated with the horizontal shear instability of the surface current, mode *B*, is independent of the topographic slope seems to be in contrast with Poulin and Flierl (2005). Indeed, this study determined that a barotropic coastal current is stabilized by a steep shelf. For simplicity we use the same velocity profile in both layers but with a much weaker amplitude in the lower layer.

In Fig. 14, we plot the growth rate curves for the two-layer RSW model with To $= -17$ and a lower-layer velocity equal to 10% (Fig. 14b), 20% (Fig. 14c), and 30% (Fig. 14d) of the upper layer. An increase in lower-layer velocity is equivalent to an increase in the barotropic component of the mean coastal flow. In Fig. 14a, we include Fig. 9h to facilitate comparison with a motionless lower layer. Introducing weak mean flows in the lower layer does not change the growth rate curves significantly. For large topographic parameters, mode *B*

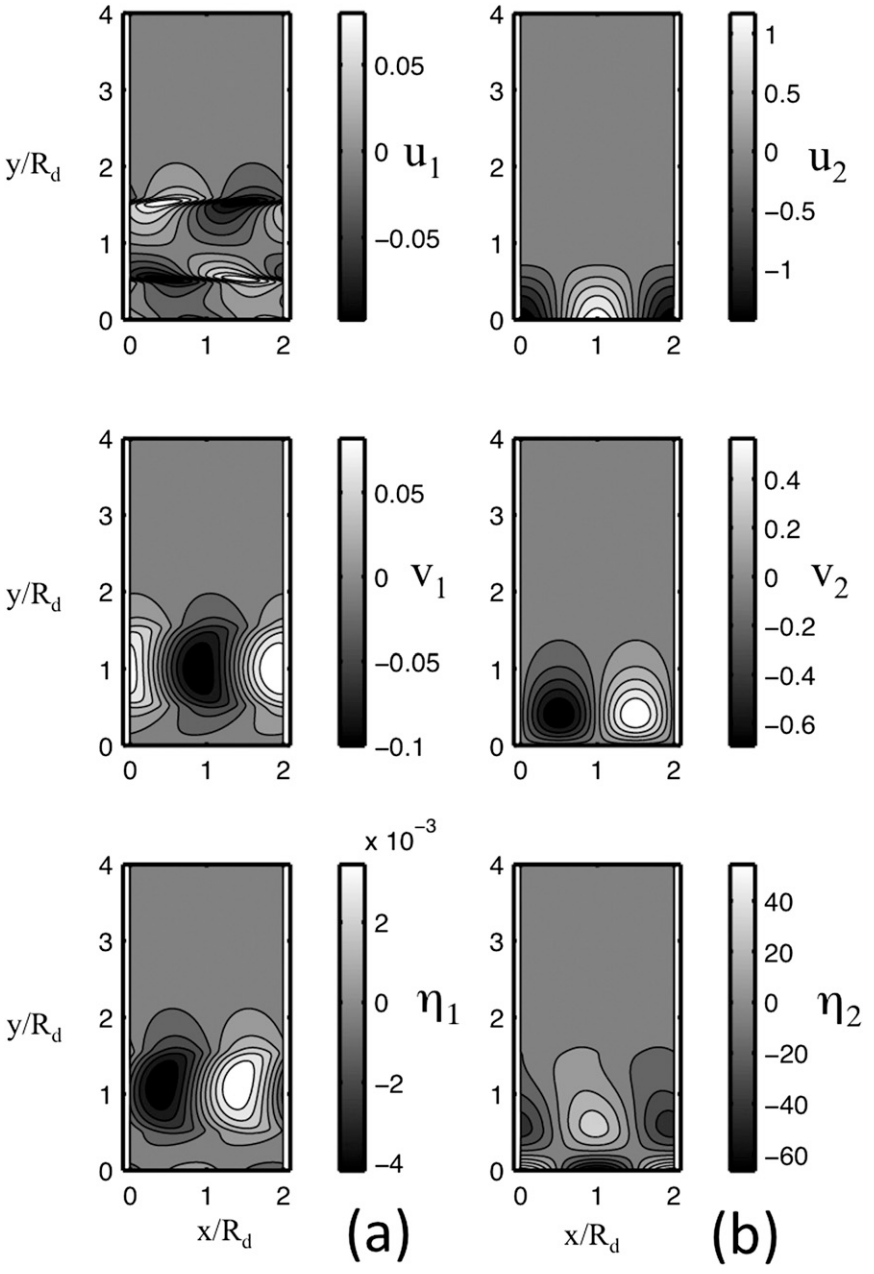

FIG. 13. Spatial structure of the most unstable mode A corresponding to $kR_d = 2.7$, the open square in Fig. 9h: (a) upper and (b) lower layers of the RSW model with To $= -17$ for the (top) alongshore velocity field, (middle) cross-shore velocity field, and (bottom) interfacial displacements.

is still the most unstable mode. In other words, the horizontal shear instability is dominant in comparison with the baroclinic instability. Quantitatively, we observe a reduction in all of the unstable growth rates through introducing a lower-layer current. The percentage of the reduction of the growth rate is approximately equal to the percentage of the lower-layer mean flow. Also, we observe a slight shift in the baroclinic wavelength selection toward smaller scales. From this we can deduce that the impact of a weak mean flow will not affect the previous results, to first order of approximation.

We have checked that even in cases where the amplitude of the lower-layer velocity is 60% of that of the upper layer, the growth rates of mode B is not affected by the bottom slope. To measure, for large To, a significant stabilization of the upper-layer mode B, we need to

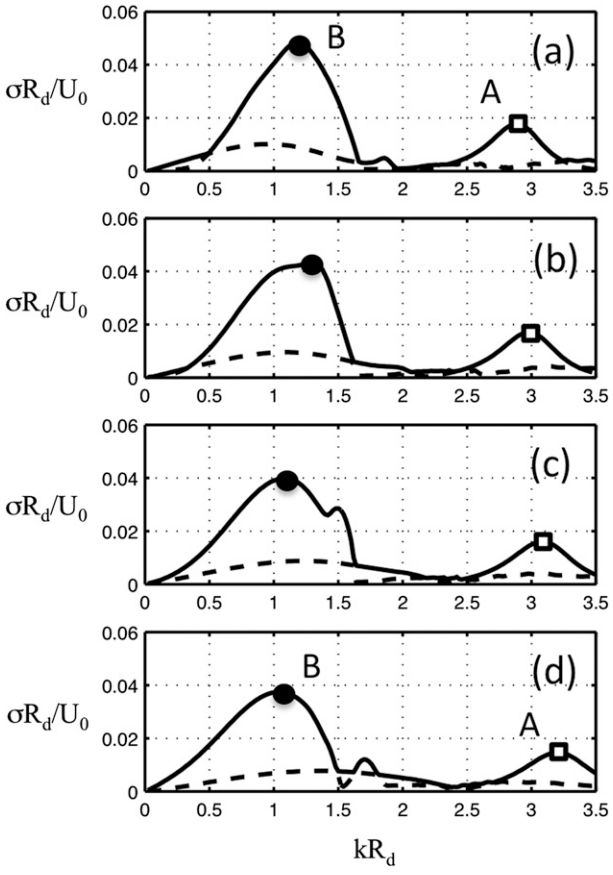

FIG. 14. The dimensionless growth-rate curves as a function of dimensionless wavenumber are plotted for the two-layer RSW model with (a) a mean velocity in the lower layer, and a lower-layer velocity equal to (b) 10%, (c) 20%, and (d) 30% of the upper layer. For (a)–(d) the topographic parameter is To = −17.

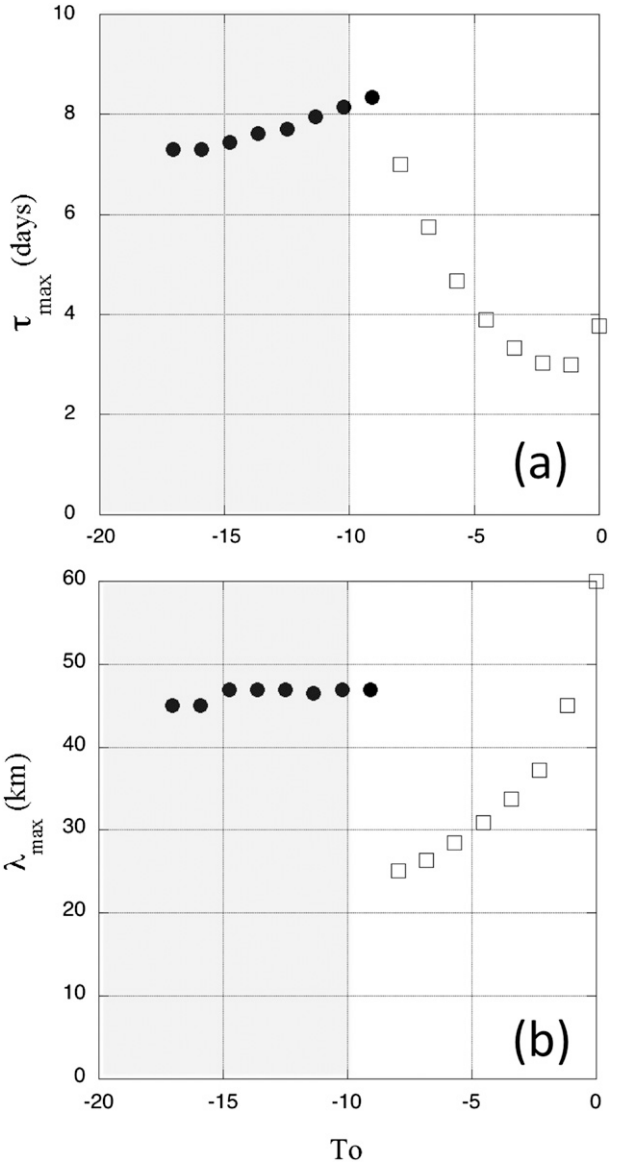

FIG. 15. Impact of the topographic parameter To on the (a) characteristic *e*-folding time in days and the (b) wavelength in kilometers of the most unstable perturbation of the idealized Bransfield Current. The open squares (filled circles) correspond to perturbations associated with baroclinic instability (horizontal shear instability). The gray region on the left corresponds to the range of parameters that are relevant for the coastal Bransfield Current.

have an almost barotropic flow with $U_2 = 0.8U_1$. Hence, the fact that the bottom topography has a weak impact on the characteristics of the horizontal shear instability, unlike the barotropic case studied in Poulin and Flierl (2005), is due to the baroclinic nature of the flow in that it is surface intensified.

5. Discussion

To apply our idealized linear stability analysis to the coastal Bransfield Current, we compute the *e*-folding time $\tau_{\max} = 1/\sigma_{\max}$ (i.e., the characteristic growth time) and the wavelength $\lambda_{\max} = 2\pi/k_{\max}$ of the most unstable perturbation as a function of the topographic parameter To. In Fig. 15, both $\tau_{\max}$ and $\lambda_{\max}$ are plotted in dimensional units: days and kilometers, respectively. We note that in the range $-20 \le \text{To} \le -10$ (denoted by a gray area), which is relevant for the Bransfield Current, the growth time is $\tau_{\max} \simeq 7.7$ days and the alongshore scale is $\lambda_{\max} \simeq 47$ km for the most unstable perturbations. These values are only weakly affected by the bottom slope in that they remain almost constant. Hence, these instability characteristics could be applied all along the SSI shelf, even if the local values of the isopycnal slopes α and the shelf slopes s may vary in time and space. This striking result finds its explanation in the fact that the steepness of the shelf slope dampens the standard baroclinic instability of the coastal current, and hence

the horizontal shear instability becomes the dominant one. According to our analysis (section 4c) this later mechanism of instability is associated with the unstable mode *B* (filled circles in Fig. 15), and we have found that the signature of this eigenmode is predominantly located in the surface layer for a surface-intensified current. Therefore, this dominant mode hardly feels the bottom topography.

The value $\lambda_{\max} \simeq 47$ km should be compared to the length of the Bransfield Strait, which is ~200 km long. Hence, there is enough space for the growth of three or four unstable meanders along the south shelf of the South Shetland Islands. However, the value $\tau_{\max} \simeq 7.7$ days is on the order of a typical transit time (~1 week) of a water parcel flowing along the SSI shelf. This slow *e*-folding time is presumably too weak to develop significant instabilities. Indeed, if we consider a purely convective instability, as in the parallel shear wake flow studied by Perret et al. (2006b,a), a small-amplitude perturbation will be amplified but will also be advected by the mean flow. Hence, in order to form a large-scale meander, an initially small but unstable wave packet perturbation should have a relatively rapid growth time $\tau_{\max}$ in comparison with the transit time along the shelf. In the present case, where $-20 \leq \mathrm{To} \leq -10$, these two characteristic time scales are of the same order of magnitude and prevent a significant growth of unstable meanders. However, for smoother shelf slopes $-5 \leq \mathrm{To} \leq 0$, the characteristic *e*-folding time will be roughly 3 days, which is typical of strongly unstable oceanic currents such as the Gulf Stream (Dimas and Triantafyllou 1995). Hence, the apparent stability of the coastal Bransfield Current is mainly due to the large negative value of the relative shelf slope (i.e., the topographic parameter To).

Consequently, the system of mesoscale warm-core anticyclonic eddies, observed in the Bransfield Strait (Fig. 14 in Sangra et al. 2011), is more likely generated by the instability of the peninsula front. Indeed, this buoyant density front, located in the center of the basin, does not flow over a steep bathymetry and is therefore expected to be more unstable than the coastal Bransfield Current. However, this hypothesis should be confirmed with a more specific survey or remote sensing analysis able to detect the generation stage of these warm-core eddies.

We are aware that our idealized two-layer model is limited in its scope. Other important mechanisms that should affect the dynamics of a density-driven current such as the coastal Bransfield Current are: 1) bottom dissipation, 2) continuous stratification, 3) temporal variability, and 4) nonlinear effects.

We have noticed that the baroclinic mode *A* has a strong signature in the bottom-layer velocity near the coast (see Fig. 12c), and therefore we expect that including bottom dissipation in the model would reduce the growth rate of this unstable perturbation. On the other hand, the unstable mode *B* associated with the horizontal shear instability of the surface current could grow even if the lower layer is motionless or strongly dissipated. Therefore, including bottom drag would presumably strengthen the dominance of the barotropic shear instability of coastal currents flowing along steep continental shelves.

We should also note that the two-layer model is a trivialization of the vertical flow structure. However, in a continuously stratified model we have no reason to believe that there will be new modes of instability that are more unstable than the two dominant modes that we have described in this paper. Hence, we can expect some quantitative changes on the growth rates and the wavenumber selection, but it should not change the main conclusion of our investigation: the stabilization of the baroclinically unstable mode above a steep shelf will lead to the dominance of the horizontal shear instability.

So far the analysis of the in situ observations focuses on the characteristics of the mean, steady surface current. There are, of course, temporal variations associated with this flow that have not been fully quantified yet. These variations could be due to tidal forcing, seasonal variability, or wind forcing. The stability characteristics of baroclinic shear flows over a flat bottom that vary in time have been computed in the context of both the linear (Poulin 2010) and nonlinear (Poulin et al. 2010) regimes. It was determined in the former that the presence of time variations can destabilize a flow but when the variations are irregular the result is more typically to stabilize the flow. We surmise that if temporal variations in the coastal Bransfield Current were included, it would likely lead to reduced growth rates, but further analysis is needed to better estimate the impact of regular or irregular forcing on coastal currents.

It is well known that the linear stability analysis is limited in that it cannot predict the final amplitude of unstable meanders. Previous studies have shown that bottom topography has a strong impact on the nonlinear saturation of unstable surface flows. Sutyrin et al. (2001) showed that even a weak bottom slope can significantly modify the eddy formation and subsequent shedding in a Gulf Stream–type jet. In particular, they show that surface meanders generate deep eddies that provide a feedback on the meander growth. In this study the bottom slope constrains the development of eddies and therefore reinforces the nonlinear saturation, which reduces the final amplitude of the meanders. Moreover, a numerical and experimental study of buoyant coastal fronts over linear shelf slopes (Pennel et al. 2012) shows

that there are no large meanders or any eddy detachments for moderate values of the topographic parameter To ≈ -3. This is evidence that the nonlinear saturation of the linear instability becomes important where the topographic slopes are comparable to the isopycnal slopes. A complete stability analysis of the Bransfield Current configuration will be performed in a future work to determine the impact of the nonlinear saturation on the unstable modes.

Acknowledgments. We express our gratitude to the technical staff and crew of the R/V *Hespérides* for supporting our work at sea. The oceanic survey was supported by the Spanish government through projects BREDDIES (REN2001-2650) and COUPLING (CTM2008-06343-CO2-01). The theoretical study was mainly supported by the France Canada Research Fund (FCRF) and the ANR-Astrid Project SYNBIOS (ANR 11 ASTR 014 01). FJP would like to thank NSERC for financial support during the research and writing of this manuscript. We thank the Field Institute for travel support during the thematic program on mathematics of oceans.

APPENDIX

Phase Locking of Rossby Waves between Two Uncoupled QG Layers with Linear Bottom Slope

In what follows, we consider two uncoupled quasi-geostrophic layers with a constant and uniform velocity in the upper one $U_1 = U_0 =$ Constant and a lower layer at rest $U_2 = 0$ with a linear bottom slope s. The phase speeds for the Rossby wave in the upper and the lower layer are given by

$$c_1 - U_1 = -\frac{H_1 R_d^2 \partial_y Q^1}{1 + R_d^2 k^2} \quad \text{and} \tag{A1}$$

$$c_2 = -\frac{H_2 R_d^2 \partial_y Q^2}{\gamma + R_d^2 k^2}. \tag{A2}$$

In this simplified case, the potential vorticity gradients are constant values:

$$\partial_y Q^1 = \frac{U_1}{H_1 R_d^2} \quad \text{and} \tag{A3}$$

$$\partial_y Q^2 = -\frac{\gamma U_1}{H_2 R_d^2} + \frac{f_0}{H_2^2} s. \tag{A4}$$

Using the geostrophic balance condition for the upper layer we get

$$f_0 U_1 = -g' \partial_y H_1 = g' \alpha, \tag{A5}$$

and therefore

$$f_0 R_d^2 s = T_0 U_1 H_1. \tag{A6}$$

The phase-speed locking is a necessary condition for the unstable growth of two Rossby waves located in the upper and lower layers, respectively. This condition of phase-speed locking $c_1(k) = c_2(k)$ leads to an implicit relation between kR_d and T_0:

$$U_1 - \frac{U_1}{1 + k^2 R_d^2} = \frac{1}{\gamma + k^2 R_d^2} \left(\gamma U_1 - \frac{f_0 R_d^2}{H_2} s \right), \tag{A7}$$

$$U_1 \left(1 - \frac{1}{1 + k^2 R_d^2} \right) = \frac{\gamma U_1}{\gamma + k^2 R_d^2} (1 - T_0), \quad \text{and} \tag{A8}$$

$$k^2 R_d^2 = \frac{\gamma (1 + k^2 R_d^2)}{\gamma + k^2 R_d^2} (1 - T_0). \tag{A9}$$

Note that for positive T_0, which corresponds to an upwelling configuration, the phase-speed locking is not possible when $T_0 \geq 1$. In this range of parameter we get a complete stabilization of the baroclinic instability. Such case never occurs for coastal current configuration ($T_0 \leq 0$).

REFERENCES

Basterretxea, G., and J. Aristegui, 1999: Phytoplankton biomass and production during late austral spring (1991) and summer (1993) in the Bransfield Strait. *Polar Biol.,* **21,** 11–22.

Bjork, G., B. Gustafsson, and A. Stigebrandt, 2001: Upper layer circulation of the Nordic seas as inferred from the spatial distribution of heat and freshwater content and potential energy. *Polar Res.,* **20,** 161–168.

Blumsack, S., and P. Gierasch, 1972: Mars: The effects of topography on baroclinic instability. *J. Atmos. Sci.,* **29,** 1081–1089.

Bowen, A., and R. Holman, 1989: Shear instabilities of the mean longshore current. *J. Geophys. Res.,* **94** (C12), 18 023–18 030.

Bracco, A., and J. Pedlosky, 2003: Vortex generation by topography in locally unstable baroclinic flows. *J. Phys. Oceanogr.,* **33,** 207–219.

——, ——, and R. Pickart, 2008: Eddy formation near the west coast of Greenland. *J. Phys. Oceanogr.,* **38,** 1992–2002.

Chelton, D., R. A. deSzoeke, M. Schlax, K. El Naggar, and N. Siwertz, 1998: Geographical variability of the first baroclinic Rossby radius of deformation. *J. Phys. Oceanogr.,* **28,** 434–460.

Dimas, A., and G. Triantafyllou, 1995: Baroclinic–barotropic instabilities of the Gulf Stream extension. *J. Phys. Oceanogr.,* **25,** 825–834.

Eden, C., and C. Boning, 2002: Sources of eddy kinetic energy in the Labrador Sea. *J. Phys. Oceanogr.,* **32,** 3346–3363.

Garcia, M., and Coauthors, 1994: Mesoscale variability in the Bransfield Strait region (Antarctica) during austral summer. *Ann. Geophys.,* **12,** 856–867.

Gula, J., and V. Zeitlin, 2013: Instabilities of shallow-water flows with vertical shear in the rotating annulus. *Modelling Atmospheric and Oceanic Flows: Insights from Laboratory Experiments and Numerical Simulations,* T. von Larcher and P. D. Williams, Eds., Amer. Geophys. Union, in press.

——, ——, and F. Bouchut, 2010: Instabilities of buoyancy driven coastal currents and their nonlinear evolution in two-layer rotating shallow water model. Part 2. Active lower layer. *J. Fluid Mech.,* **665,** 209–237.

Hatun, H., C. Eriksen, and P. Rhines, 2007: Buoyant eddies entering the Labrador Sea observed with gliders and altimetry. *J. Phys. Oceanogr.,* **37,** 2838–2854.

Li, S., and T. McClimans, 2000: On the stability of barotropic prograde and retrograde jets along a bottom slope. *J. Geophys. Res.,* **105** (C4), 8847–8855.

Lozier, M., and M. Reed, 2005: The influence of topography on the stability of shelfbreak fronts. *J. Phys. Oceanogr.,* **35,** 1023–1036.

——, ——, and G. Gawarkiewicz, 2002: Instability of a shelfbreak front. *J. Phys. Oceanogr.,* **32,** 924–944.

Mechoso, C., 1980: Baroclinic instability of flows along sloping boundaries. *J. Atmos. Sci.,* **37,** 1393–1399.

Millot, C., 1999: Circulation in the western Mediterranean Sea. *J. Mar. Syst.,* **20,** 423–442.

Mysak, L., 1977: On the stability of the California Undercurrent off Vancouver Island. *J. Phys. Oceanogr.,* **7,** 904–917.

Niiler, P., A. Amos, and J. Hu, 1991: Water masses and 200 m relative geostrophic circulation in the western Bransfield Strait region. *Deep-Sea Res.,* **38,** 943–959.

Obaton, D., G. Millot, G. Chabert d'Hières, and I. Taupier-Letage, 2000: The Algerian Current: Comparisons between in situ and laboratory data sets. *Deep-Sea Res.,* **47,** 2159–2190.

Paldor, N., 1983: Stability and stable modes of coastal fronts. *Geophys. Astrophys. Fluid Dyn.,* **27,** 217–228.

Pedlosky, J., 1987: *Geophysical Fluid Dynamics.* Springer-Verlag, 710 pp.

Pennel, R., A. Stegner, and K. Beranger, 2012: Shelf impact on buoyant coastal current instabilities. *J. Phys. Oceanogr.,* **42,** 39–61.

Perret, G., A. Stegner, T. Dubos, J. Chomaz, and M. Farge, 2006a: Stability of parallel wake flows in quasigeostrophic and frontal regimes. *Phys. Fluids,* **18,** 126602, doi:10.1063/1.2397563.

——, ——, M. Farge, and T. Pichon, 2006b: Cyclone–anticyclone asymmetry of large-scale wakes in the laboratory. *Phys. Fluids,* **18,** 036603, doi:10.1063/1.2179387.

——, T. Dubos, and A. Stegner, 2011: How large-scale and cyclogeostrophic barotropic instabilities favor the formation of anticyclonic vortices in the ocean. *J. Phys. Oceanogr.,* **41,** 303–328.

Phillips, N., 1954: Energy transformations and meridional circulations associated with simple baroclinic waves in a two-level quasigeostrophic model. *Tellus,* **6,** 273–286.

Pickart, S., D. Torres, and P. Fratantoni, 2005: The East Greenland Spill Jet. *J. Phys. Oceanogr.,* **35,** 1037–1053.

Poulin, F., 2010: The linear stability of aperiodic baroclinic shear. *J. Phys. Oceanogr.,* **40,** 568–581.

——, and G. Flierl, 2003: The nonlinear evolution of barotropically unstable jets. *J. Phys. Oceanogr.,* **33,** 2173–2192.

——, and ——, 2005: The influence of topography on the stability of jets. *J. Phys. Oceanogr.,* **35,** 811–825.

——, ——, and J. Pedlosky, 2010: The nonlinear dynamics of aperiodic baroclinic shear. *J. Phys. Oceanogr.,* **40,** 1851–1865.

Puillat, I., I. Taupier-Letage, and C. Millot, 2002: Algerian eddies lifetime can near 3 years. *J. Mar. Syst.,* **31,** 245–259.

Sakai, S., 1989: Rossby Kelvin instability: A new type of ageostrophic instability caused by a resonance between Rossby waves and gravity waves. *J. Fluid Mech.,* **202,** 149–176.

Sangra, P., and Coauthors, 2011: The Bransfield Current System. *Deep-Sea Res.,* **58,** 390–402.

Savidge, D., and J. Amft, 2009: Circulation on the west Antarctic Peninsula derived from 6 years of shipboard ADCP transects. *Deep-Sea Res.,* **56,** 1633–1655.

Sutyrin, G., I. Ginis, and S. Frolov, 2001: Equilibration of baroclinic meanders of deep eddies on a Gulf Stream–type jet over a sloping bottom. *J. Phys. Oceanogr.,* **31,** 2049–2064.

Trefethen, L., 2000: *Spectral Methods in Matlab.* SIAM, 165 pp.

Vallis, G., 2006: *Atmospheric and Oceanic Fluid Dynamics: Fundaments and Large-Scale Circulation.* Cambridge Press, 768 pp.

Zeitlin, V., 2007: *Nonlinear Dynamics of Rotating Shallow Water: Methods and Advances*. Elsevier, 400 pp.

Zhou, M., P. Niiler, and J. Hu, 2002: Surface currents in the Bransfield and Gerlache Straits, Antarctica. *Deep-Sea Res.,* **49,** 267–280.

——, ——, Y. Zhu, and Y. Dorland, 2006: The western boundary current in the Bransfield Strait, Antarctica. *Deep-Sea Res.,* **53,** 1244–1252.